One-step, low temperature synthesis of reduced graphene oxide decorated with ZnO nanocrystals using galvanized iron steel scrap

Tolentino-Hernandez, R V; Jimenez-Melero, E.; Espinosa-Faller, F J; Guarneros-Aguilar, C; Caballero-Briones, F

DOI:
10.1088/2053-1591/ac0c9c

PAPER • OPEN ACCESS

One-step, low temperature synthesis of reduced graphene oxide decorated with ZnO nanocrystals using galvanized iron steel scrap

Materials Research Express

PAPER

One-step, low temperature synthesis of reduced graphene oxide decorated with ZnO nanocrystals using galvanized iron steel scrap

R V Tolentino-Hernandez[1], E Jimenez-Melero[2], F J Espinosa-Faller[3], C Guarneros-Aguilar[4] and F Caballero-Briones[1,*]

[1] Instituto Politécnico Nacional, Materiales y Tecnologías para Energía, Salud y Medio Ambiente (GESMAT), CICATA Altamira. Km 14.5 Carretera Tampico-Puerto Industrial Altamira, 89600 Altamira, México
[2] School of Materials, The University of Manchester, Manchester M13 9PL, United Kingdom
[3] Escuela de Ingeniería, Universidad Marista de Mérida, Mérida, Yucatán, 97300, México
[4] CONACYT- Instituto Politécnico Nacional, Materiales y Tecnologías para Energía, Salud y Medio Ambiente (GESMAT), CICATA Altamira. Km 14.5 Carretera Tampico-Puerto Industrial Altamira, 89600 Altamira, México
* Author to whom any correspondence should be addressed.

E-mail: fcaballero@ipn.mx

Keywords: ZnO-rGO, galvanic displacement, spontaneous reaction, GO reduction

OPEN ACCESS

RECEIVED
14 April 2021

REVISED
7 June 2021

ACCEPTED FOR PUBLICATION
18 June 2021

PUBLISHED
30 June 2021

Abstract

Production of a ZnO–rGO composite, using a novel one-pot method consisting in continuously flowing argon into a GO aqueous suspension heated at 80 °C, in the presence of galvanized iron steel scrap is presented. FTIR shows the complete disappearance of GO functional groups and only the C=C band remained, indicating extensive GO reduction. Raman spectra indicated sp^2 character increase after reaction and the presence of the E_{2h} mode of ZnO. SEM showed submicron crystals identified by XRD as ZnO in the hexagonal phase, while TEM images indicate ZnO nanoparticles decorate mainly the rGO borders. Optical band gap of 3.5 eV corresponding to ZnO, and optical transitions at 4.1 and 5.5 eV related with $n \rightarrow \pi$ and $\pi \rightarrow \pi^*$ were observed. Electrochemical characterization by cyclic voltammetry shows an specific capacitance of 4.7 F g^{-1} at a scan rate of 5 mVs^{-1}, which drops to ca. 0.8 F g^{-1} at 200 mVs^{-1}. By electrochemical impedance spectroscopy, the relaxation time was ca. 5 ms. The proposed mechanism for the materials' synthesis includes Zn dissolution from scrap, galvanic displacement of oxygen moieties at the GO sheet, Zn deposition onto the carbon surface, and further oxidation and growth of ZnO nanocrystals.

1. Introduction

Graphene oxide (GO) and reduced graphene oxide (rGO) have been attractive in the development of new materials for technological applications as optoelectronic devices [1–3], chemical sensors [4], photovoltaic materials [5], energy storage [6] and composite materials [7, 8] due to its excellent optoelectronic, mechanical, thermal, and electrical properties. The production of reduced graphene oxide from chemically derived graphene oxide (GO) has been extensively studied. Approaches such as the addition of strong and mild reducing agents such as hydrazine, sodium borohydride or active metals, as well as the use of reducing sugars, citric acid and other green methods, thermal reduction and two step reduction routines, have been reported [9–11].

With respect to the reduction of GO using Zn powder, Mei and Ouyang [12] reported GO reduction at room temperature using Zn powder and ultrasonication at pH 2 adjusted with HCl; the authors report the almost complete removal (yet incomplete) of functional groups and traces of Zn in the resulting material. The authors suggest an electrochemical mechanism for GO reduction. Pei *et al* [13] also reported GO reduction with Zn powder but the FTIR spectra shows the presence of methyl-methylene groups indicating rupture of the aromatic character. Both authors point out the extent of reduction in dependence of the Zn/GO ratio. In another contribution, Sankar and Basak presented a hydrothermal method to obtain ZnO-rGO 'hybrids' using Zn powder, different amounts of GO and cetyl trimethyl ammonium bromide at 160 °C for 20 h [14]. Neither evidence on the resultant rGO degree of reduction nor of ZnO attachment onto the rGO sheet was shown. A

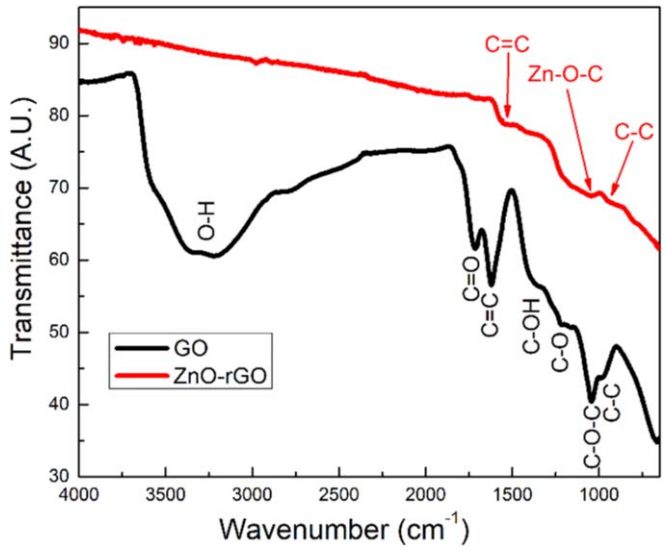

Figure 1. FTIR spectra of GO and ZnO–rGO.

mechanism for ZnO formation was proposed but not explained to elucidate the roles of the surfactant and the temperature/pressure conditions.

In the present contribution we describe an almost serendipitous finding: during the pursue for GO reduction at low temperature (80 °C) using galvanized iron steel scrap as reducing agent in the presence of Ar bubbling, reduced graphene oxide decorated with high quality ZnO crystals was obtained after only 1 h of reaction. The material's characteristics and the decoration mechanism are outlined, which lead the path to a cheaper, effective and easy way to produce ZnO–rGO materials with the possible obtention of different nanostructures to improve its performance in the actual areas of investigation.

2. Experimental details

Graphene oxide was obtained by graphite oxidation, using a modification of the Hummers method as reported elsewhere [15]. For the reduction process, 50 ml of 1 mg ml^{-1} GO aqueous suspension was sonicated for 1 h. The solution pH was 2. Later, 2 g of <1 cm cuts of galvanized iron steel scrap from a piece of G-40 alloy (0.40 Zn oz/ft^2) were added to the mixture. Afterwards temperature was raised to 80 °C while Ar was bubbled into the GO solution at a 10 sccm rate. Vigorous stirring with a Teflon magnetic bar was kept for 1 h. The solution was let to cool; the powders were recovered by centrifugation, washed in water and ethanol, and dried at 60 °C overnight. The resulting product has the typical black color of rGO; sample is named ZnO–rGO.

Fourier Transform Infrared (FTIR) spectroscopy measurements were carried out in a Perkin Elmer Spectrum 100 spectrometer in the ATR mode in the wavenumber range of 650–4000 cm^{-1}. Micro-Raman spectroscopy was performed with a HORIBA Jobin Yvon model LabRAM-HR instrument, using a He-Ne laser (632.8 nm). X-ray diffraction (XRD) measurements were performed in a Bruker D8 Advance diffractometer using Cu Kα ($\lambda = 0.15406$ nm) radiation, equipped with a Lynx Eye detector in the Bragg-Brentano configuration from 5°–85° in 2θ with step size angle of 0.02° each second and sample rotation. Morphology and composition were analyzed in a scanning electron microscope (SEM) FEI-FIB Dual Beam Helios Nanolab 600, equipped with an Energy Dispersive (EDS) detector and in a transmission electron microscope (TEM) JEOL model JEM-1010 equipped with a digital camera model ORIUS by Gatan, operated at 80 kV. UV–vis diffuse reflectance spectra were obtained in an Evolution 600 UV–vis spectrophotometer calibrated with a Spectralon® standard in the range of 200–800 nm. For the electrochemical characterization, a slurry was prepared by weighing 14 mg of the synthesized powder and mixing it with 1 mg of polyvinyl alcohol as binder and 5 mg of graphite powder, in an agate mortar and adding N-methyl-pyrrolidone to produce a thick paste. The paste was applied onto a 1 × 1 cm^2 gold-coated glass substrate and let dry overnight at 50 °C. The cyclic voltammograms (CV) and electrochemical impedance spectroscopy (EIS) were performed using a Squidstat Plus (Admiral) electrochemical station using the prepared electrode as working electrode, a rhodium-coated copper wire as auxiliary electrode and a Pt/Ir wire as pseudoreference electrode. As supporting electrolyte, a 0.1 M $NaNO_3$ solution was used.

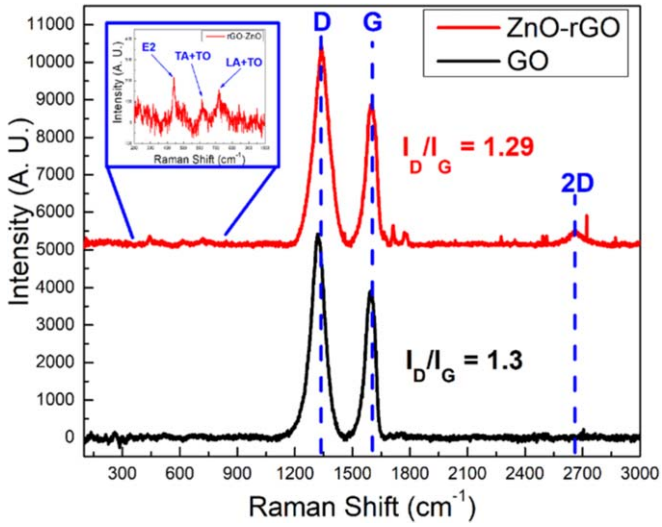

Figure 2. Raman spectrum of GO (black) and ZnO–rGO (red) samples.

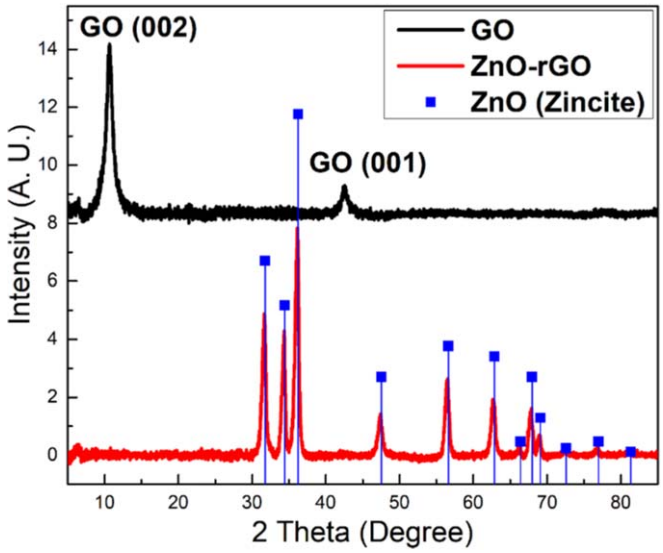

Figure 3. X-ray diffractogram of GO and ZnO/rGO powders.

3. Results and discussion

3.1. Structure and composition

In figure 1 the FTIR spectra of GO and ZnO–rGO are presented. In the GO spectrum, a strong and wide band at 3300 cm^{-1} corresponding to O-H of residual water intercalated between the graphene sheets, is observed. Bands at 1720 cm^{-1} (stretching vibration of the carboxyl group (C=O)), at 1620 and 970 cm^{-1} (C=C and C–C of the graphene skeleton), at 1375 and 1222 cm^{-1} (bending vibration and stretching of edge hydroxyl groups (C–OH)) and at 1044 cm^{-1} (epoxy (C–O–C)) are observed too, in agreement to our previously published work [15]. In the ZnO–rGO spectra, all the bands related with oxygen groups disappeared and only the bands of the graphene skeleton (C=C and C–C) are observed at 1560 and 970 cm^{-1} respectively, indicating a higher reduction degree, compared to the works of Mei [12] and Liu [13]. Also a band at 1040 cm^{-1} attributed to asymmetric stretching vibrations of bridge–oxygen in Zn–O–C is observed [16–18].

In figure 2 the Raman spectra of GO and ZnO–rGO are presented. In GO spectra, bands D and G are observed at 1319 cm^{-1} and 1594 cm^{-1} respectively, these bands are related with the defect-activated ring breathing mode vibrations A_{1g} also called disorder band, and with the vibrational mode of sp^2 bonded carbon E_{2g} or graphitic band respectively [19]. In ZnO–rGO spectra, bands D and G are also observed, as well as the 2D band at 2663 cm^{-1}. From the 2D band is possible to identify single-layer graphene and few-layer graphene [20].

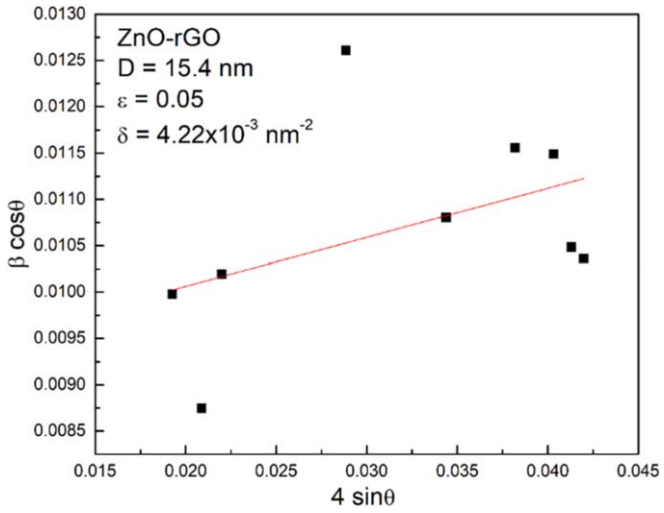

Figure 4. Williamson-Hall plot of ZnO/rGO powders.

In [12] the 2D band was also observed, indicating an increased exfoliation and restoring of the sp^2 character, although the relative intensity of the D and G bands support the loss of aromatic character denoted after methyl-methylene groups formation observed by the authors in the FTIR spectra [12]. In contrast, we did not observe the FTIR bands related with methyl-methylene groups, and the appearance of the 2D band in our material indicates the partial restoration of sp^2 domain (graphitization) [21] and exfoliation of the multilayer GO starting material to a few layered rGO [22], due to the growth of ZnO all over the surface of graphene sheets [23]. At 440 cm^{-1} the E_{2h} (high) mode associated with oxygen vibrations on the ZnO lattice is observed; the low intensity of E_{2h} Raman mode usually attributed to a high disorder on crystalline symmetry [24]. Multiphonon ZnO modes at 617 cm^{-1} and 718 cm^{-1} corresponding to TA + TO and LA + TO modes were observed too [25]. Additional non-assigned Raman bands were observed at ca. 1708 cm^{-1} and 1770 cm^{-1}, but its identity shall be elucidated in a future work.

Crystallite size (La) was estimated using I_D/I_G ratio from the Raman spectra from the formula described in [26]:

$$La(nm) = (2.4\ x\ 10^{-10})\,\lambda_L^4 (I_D/I_G)^{-1} \tag{1}$$

Where La is the crystallite size and λ_L is the wavelength of the laser source (nm). Crystallite size values were 30 nm for GO and 27 nm for ZnO–rGO.

In figure 3 the X-ray diffractograms of GO and ZnO–rGO are presented. The diffractogram of GO exhibit the characteristic peaks of the planes (002) and (001) at 2θ 10.6° and 42.5° respectively, with an interplanar distance $d_{(002)} = 0.83$ nm. For the ZnO–rGO diffractogram, the reflections observed at 2θ 31.8°, 34.4°, 36.3°, 47.5°, 56.6°, 62.9°, 66.4°, 68°, 69.1°, 72.6°, 77° and 81.4° correspond to the planes (100), (002), (101), (102), (110), (103), (200), (112), (201), (004), (202) and (104) respectively of the ZnO hexagonal wurtzite structure also known as zincite (PDF Card # 361451). The sharp diffraction peaks indicate high crystallinity of ZnO. The absence of the GO reflections in ZnOrGO is associated with the exfoliation of graphene sheets after ZnO incorporation, which reduces the sheet bundles capable of diffraction, besides the low diffraction power of carbon compared to ZnO [17, 27, 28].

Usually, to estimate the average coherent domain size, the Scherrer equation is the fastest and simple choice to do, however it can be used only for the strongest reflections [29].

$$D = \frac{k\lambda}{\beta \cos\theta} \tag{2}$$

Instead, if a more accurate result of the crystallite size and the effective lattice strain are required, the Williamson-Hall method (W-H) is the best choice; W-H plot is based in the following equation [30].

$$\beta \cos\theta = \frac{k\lambda}{D} + 4\varepsilon \sin\theta \tag{3}$$

where β in the FWHM of the diffraction peak, θ in the angle of the diffraction, k is a shape factor (0.9), λ is the wavelength of X-rays (0.154056 nm), D is the crystallite size and ε is the effective lattice strain. In Williamson-Hall method $\beta\cos\theta$ versus $\sin\theta$ is plotted (figure 4), a linear fit is made to the data in the plot, and the crystallite size (D) is obtained from the intercept, while the strain is deduced from the slope. The average crystallite size for

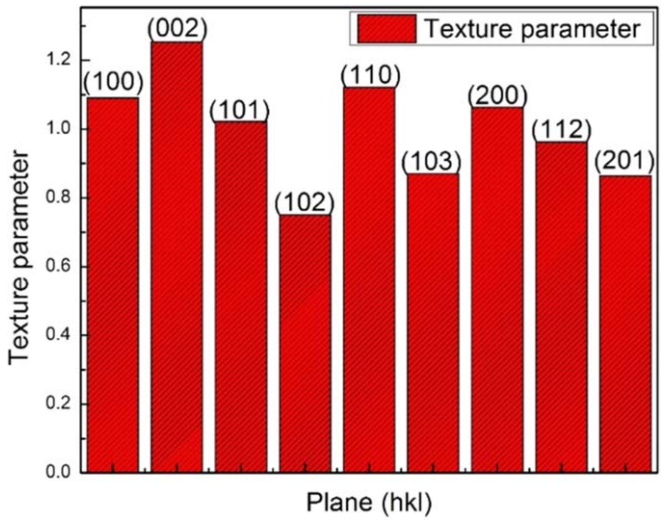

Figure 5. Texture parameter of ZnO/rGO powders.

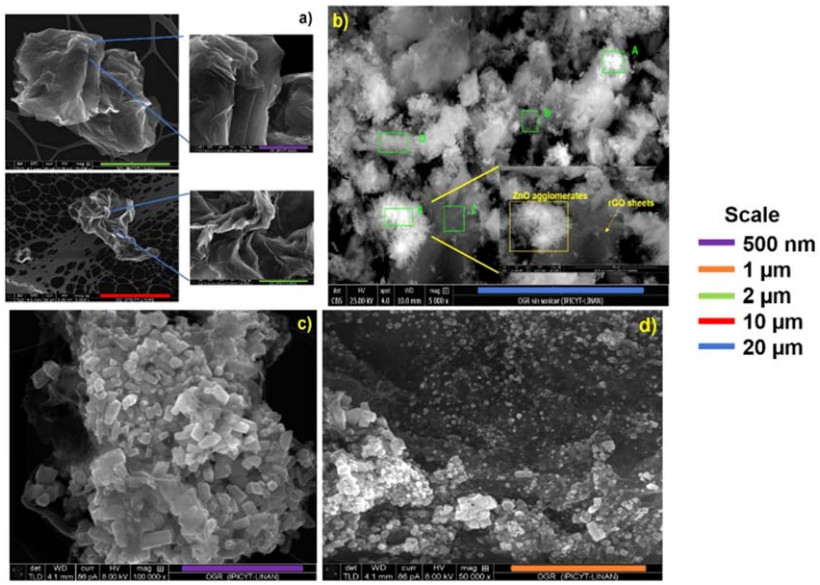

Figure 6. SEM image of (a) GO with different magnifications, (b) rGO sheets with ZnO agglomerates with a magnification of the E-C zones, (c) rGO sheets with ZnO crystals and (d) detail of ZnO particles onto the rGO sheets.

the ZnO crystals, obtained with Scherrer equation of 13.4 nm and for the W-H method, 15.4 nm. The effective strain was 0.05 to ZnO–rGO, indicating a low tensile strain, which is attributed to a low lattice mismatch between rGO and ZnO lattices, as well as to the cluster-like deposition of ZnO, discussed below [31–34].

To get a better insight about the concentration of defects present in the material structure, the dislocation density (δ) can be estimated from the crystallite size value, using the following expression [35].

$$\delta = \frac{1}{D^2} \tag{4}$$

The density of dislocations obtained for ZnO–rGO was $4 \times 10^{-3}\,\mathrm{nm}^{-2}$.

The relative intensity of each diffraction plane (hkl) of the material can be defined to assess the degree of a specific crystal facet exposure, which is called texture parameter ($T_{(hkl)}$) and is given by [36].

$$T_{(hkl)} = \frac{\frac{I_{(hkl)}}{I_{0(hkl)}}}{\frac{1}{N}\sum_{1}^{N}\left(\frac{I_{(hkl)}}{I_{0(hkl)}}\right)} \tag{5}$$

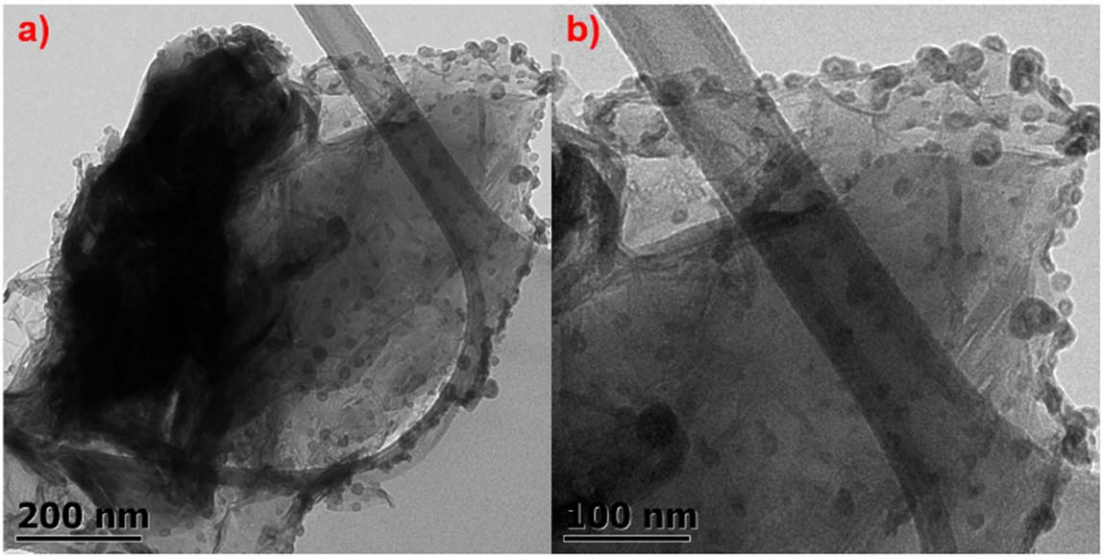

Figure 7. TEM micrographics of ZnO–rGO (a), (b).

Table 1. Elemental composition of ZnO–rGO in wt.% from EDS data.

Zone element	A	B	C	D	E	**Mean**	SD (error)
C	19.74	36.74	49.77	35.22	22.74	**32.842**	12.05321
O	34.04	30.46	26.61	25.05	32.44	**29.72**	3.81082
Zn	44.49	31.47	21.29	38.20	42.81	**35.652**	9.4815
Al	1.62	0.77	0.44	0.92	1.76	**1.102**	0.56632
Fe	0.11	0.37	0.69	0.25	0.17	**0.318**	0.22961
Cu	—	0.2	1.2	0.36	—	**0.58667**	0.53715

where $I_{(hkl)}$ and $I_{0(hkl)}$ are the intensities of the (hkl) experimental diffraction peaks and the intensity of correspondent to standard polycrystalline randomly oriented XRD pattern (PDF Card # 361451), N the number of peaks used for the operation. In figure 5 the texture parameters of each plane in the ZnO–rGO diffractogram are presented. The material has almost the powder texture, only the plane (002) trends a slight preferential orientation above the other planes, in accordance with the morphology observed by SEM and TEM as discussed below, where some hexagonal rods with (002) habit are observed [37, 38].

Figure 6 presents different SEM images of the GO and ZnO–rGO samples. In figure 6(a), corrugated and exfoliated GO sheets with size of 1–10 μm are observed. The EDS data corresponding to the GO sheet indicate a composition of 78% C and 22% O corresponding to the typical values of GO produced in our Group [15]. In figure 6(b) multiple agglomerates of ZnO rods are observed onto the rGO sheets, in this image, EDS spectra were taken in the zones (A-E) marked in green squares and the elemental composition is given in table 1. In figure 6(c) a magnification of the ZnO particles onto rGO sheets is presented: as in figure 6(b), agglomerates of ZnO with different sizes and length-diameter proportions are observed. Figure 6(d) shows ZnO crystals directly nucleated onto the rGO sheet. A more detailed explanation of the ZnO growth mechanism onto rGO is discussed below.

The composition depicted in table 1 shows a mean Zn content of ca. 36 wt%, a maximum of 0.3 wt% of Fe from the galvanized iron scrap and 1.7 wt% of other metal impurities such as Al and Cu, from the G-40 scrap and from the sample holder. Carbon accounts for ca. 33 wt. % of the mean composition.

In figure 7 TEM micrographs were taken for further analyze the morphology features of ZnO grown on the rGO sheets. In figure 7(a) the presence of nanoparticles decorating the rGO sheet borders and surface is observed. From the figure 7(b) at higher magnification, it can be seen that the ZnO nanoparticles are dense, but the particle sizes are not uniform, attributed to a continuous nucleation as described in the reaction mechanism below. The strong attachment of the particles to the rGO sheet is proved, as after sonication during preparation for TEM, the ZnO remain attached to the sheets.

3.2. Optical and electrochemical behavior

Diffuse reflectance spectra of ZnO–rGO is presented in figure 8. The absorption peak of the ZnO asigned to its band gap is usually reported around 355 nm [30, 39]. In figure 8(a) the absorption peak attributed to ZnO–rGO

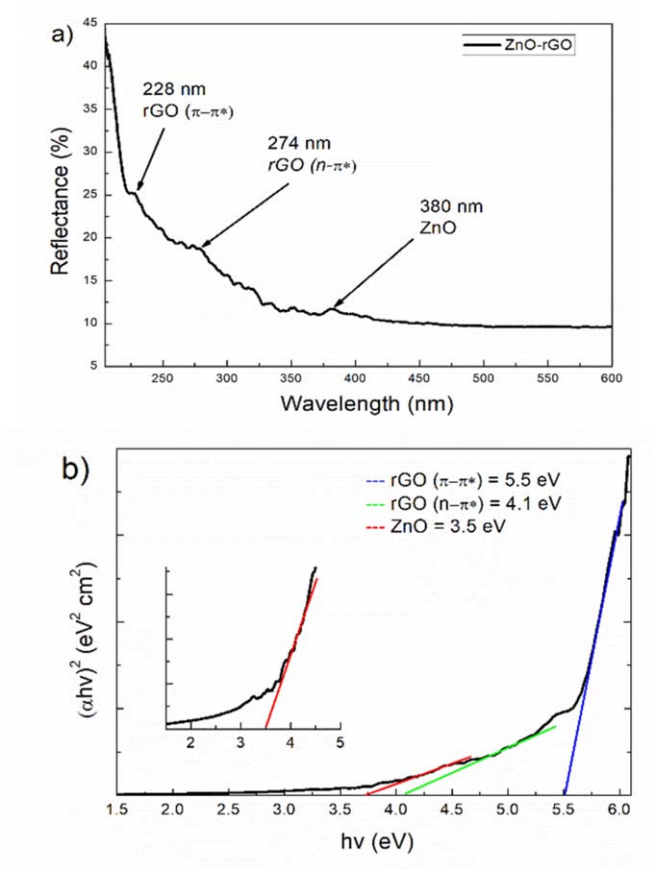

Figure 8. UV–vis absorption spectra of (a) ZnO–rGO and (b) Tauc plot.

appears in 380 nm; the observed red shift is related to the contribution of carbon atoms to ZnO [40–42]. The absorbance at 274 nm and 228 nm which are ascribed to n $\rightarrow \pi^*$ and $\pi \rightarrow \pi^*$ optical transitions that are due to plasmon effect of C–C bond in graphitic structure and of the sp2 bonding of C=C from benzenic ring in rGO materials respectively [43–46].

From the reflectance spectra the direct band gap was calculated using the Tauc relationship. In figure 8(b) the (αhv)2 versus hv plot is shown; the linear regions were fitted to y = 0 [31] to calculate the value of the ZnO band gap and the rGO electronic transitions (n–π^* and π–π^*). The band gap of ZnO is 3.5 eV and the energies calculated for the optical transitions of rGO were 4.1 eV for n–π^* and 5.5 eV for π–π^* respectively [47, 48].

Figure 9 presents the electrochemical characterization of an electrode prepared with the synthesized ZnO–rGO powder. Figure 9(a) presents the cyclic voltammetry (CV) plots of the ZnO–rGO electrode recorded at a scan rates of 5, 10, 20, 50, 100 and 200 mV s^{-1} in the −1.0 to 1.0 V versus OCP (open circuit potential). CV curves are repetitive and exhibit a capacitive behavior as noticed by a typical rectangular CV curve.

Small faradaic response around 0.3 and −0.3 V versus SSC was observed in the chosen voltage window ascribed to the response of the electrical doble layer capacitance (EDLC) and a pseudocapacitance response of the materials [49]. From the integration of the CV curves the specific capacitance (C_{cp}) was calculated by the following expression [50, 51]:

$$C_{sp} = \frac{A}{m\upsilon\Delta V} \tag{6}$$

where C_{sp} is capacitance, A the integral area of CV curves, m is the active mass of the material in g, υ scan rate in V s^{-1} and ΔV the voltage window in volts [52–54].

As is seen in table 2 the current increases with the scan rate; instead the specific capacitance decreases. The behavior is explained as at higher scan rates the contact between electrolyte and electrode surface occurs for a very short time so less electrolyte penetrates into the electrode pores and then less contact with internal surface, au contraire, at low scan rates the ions have more time to penetrate the pores, leading to the increased capacitance. In figure 9(b), the specific capacitance against the scan rate is presented [55].

EIS is useful tool for evaluate the electrochemical performance of a material as electrode. Figure 9(c) presents the Nyquist plot of ZnO–rGO. In the lower right corner inset of figure 9(c), a zoom of the semicircle of Nyquist

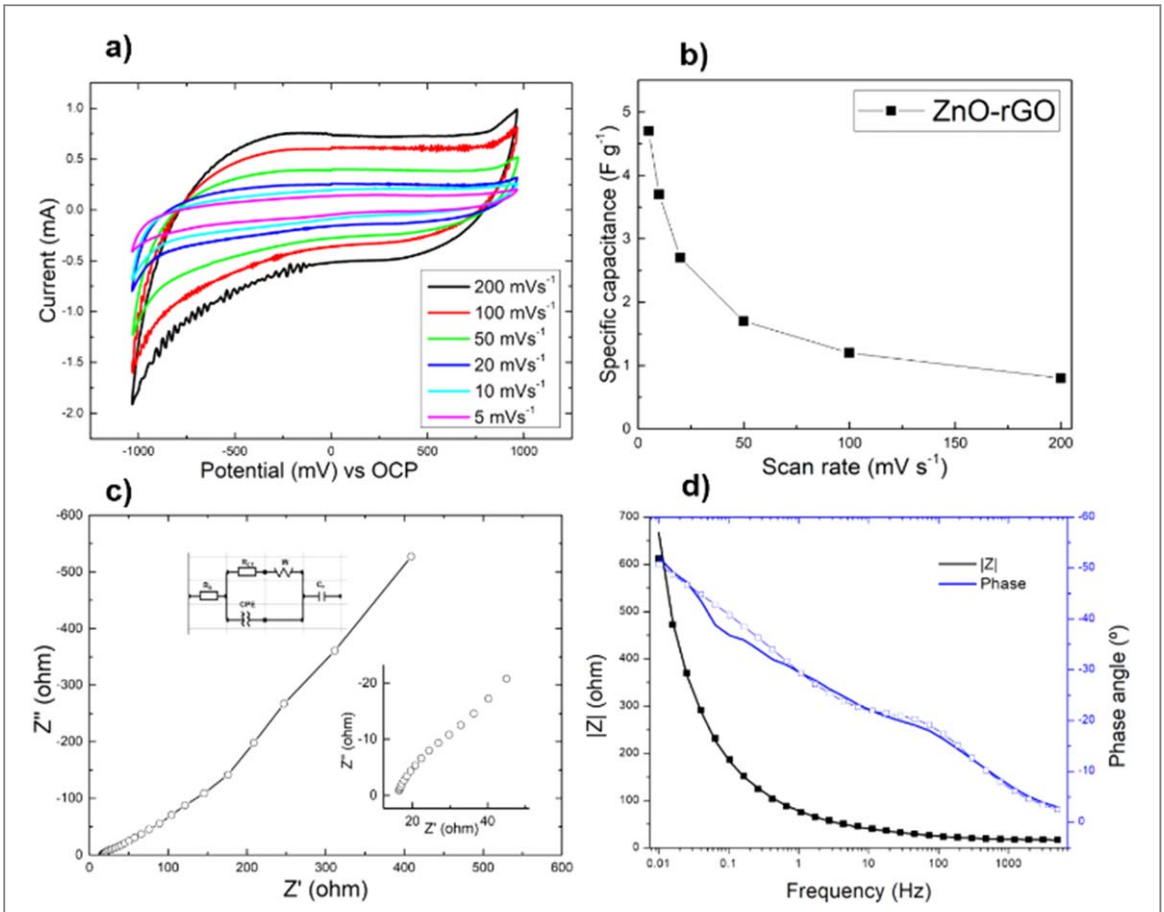

Figure 9. (a) CV curves of the and ZnO–rGO electrodes measured at different scan rates (5, 10, 20, 50, 100 and 200 mV s^{-1}), (b) specific capacitance against scan rate plot, (c) nyquist plot of ZnO–rGO, the equivalent circuit in the upper left corner inset and a zoom of the semicircle of Nyquist plot at high frequencies in the lower right corner inset, respectively and (d) bode plot.

Table 2. Specific capacitance at scan rates of 5 to 200 mV s^{-1} of ZnO–rGO.

Scan rate (mV s^{-1})	Current (mA)	Specific capacitance (F g^{-1})
5	0.33	4.7
10	0.52	3.7
20	0.75	2.7
50	1.21	1.7
100	1.71	1.2
200	2.22	0.8

plot is presented. This semicircle is usually attributed to the EDLC of rGO materials, followed by a resistive behavior [45, 46, 56, 57]. The equivalent circuit model proposed to analyze the impedance data is shown in the upper left corner inset of figure 8(b). In the circuit, R_S represents the series resistance, which includes the electrolyte resistance, interface resistance between bulk electrode and electrolyte, and the current collector; R_{CT} is the charge transfer resistance of the electrode; CPE is the constant phase element related to double layer capacitance, usually used instead classical capacitance due to surface inhomogeneity; C_F is a pseudocapacitance and W is Warburg impedance from ionic diffusion [58]. From the circuit fitting, R_S value is 16Ω and R_{CT} 26.7Ω, CPE is 868 μF, C_F is 145.5 $\times$ 10^3 μF and W is 7.49 $\times$ 10^{-3}; the series resistance of our ZnO–rGO material result less than the reported in [59]. Figure 9(d) shows the Bode plot of ZnO–rGO (|Z| and phase versus log f). At high frequencies and with a phase angle near to zero correspond to R_S, moreover, two peaks in the middle and low frequency range would correspond to the electron transfer resistance and diffusion within the electrolyte [60]. An interesting feature to evaluate in supercapacitor applications is f_0, the phase angle of 45° where the resistive and capacitive impedances are equivalent, also known as the relaxation time, and refers to the shortest time necessary to discharge the whole energy of the material with an efficiency larger than 50%. The calculation of f_0 is given by the following expression:

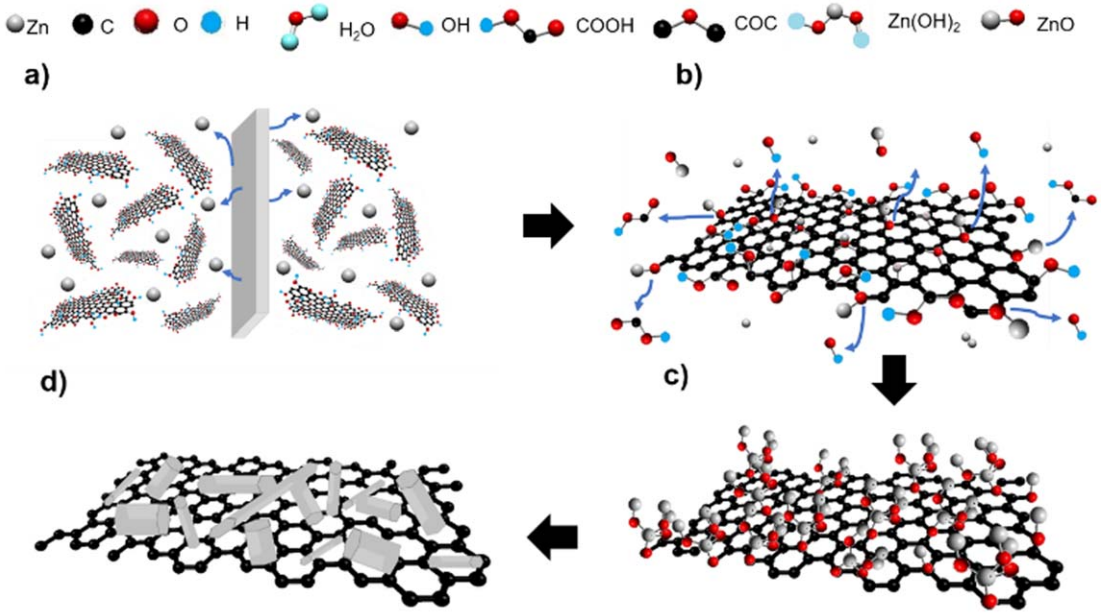

Figure 10. Scheme of the reaction mechanism for ZnO–rGO, (a) sacrificial dissolution of Zn atoms from galvanized iron in the presence of GO dissolution; (b) galvanic displacement of oxygen groups by Zn^{2+}; (c) formation of ZnO nuclei by effect of temperature and growth of ZnO crystals and (d) resultant ZnO–rGO material.

$$\tau_0 = \frac{1}{f_0} \tag{7}$$

where τ_0 is the relaxation time and f_0 the frequency at phase angle of 45°, which is 4.95 ms to our material [61, 62].

3.3. Reaction mechanism

The reaction mechanism proposed for the synthesis of the ZnO–rGO powder using galvanized iron scrap, is the following: first the metallic Zn atoms present on the galvanized iron scrap dissolve in contact with GO aqueous dispersion at pH 2, as follows [63]:

$$MZn + GO + H_2O \xrightarrow{pH\ 2} M + Zn^{2+} + GO^{-} + H_2O \tag{8}$$

The active Zn ion hydrates at low pH; the standard redox potential for Zn^0/Zn^{2+} is $E^0 = 0.7618$ V [64, 65], GO deprotonates when is dispersed in water. By the effect of temperature the homogeneous formation of $Zn(OH)_2$ and then ZnO can occur in the solution [17, 66]:

$$Zn - 2e^{-} + GO + H_2O \rightarrow Zn^{2+} + GO^{-} + H^{+} + H_2 \uparrow + 2OH^{-} \tag{9}$$

$$Zn^{2+} + OH^{-} \rightarrow Zn(OH)_2 \rightarrow ZnO + H_2O \tag{10}$$

The heterogeneous nucleation and growth of ZnO on reduced GO layers is proposed to occur in two stages, (i) a spontaneous galvanic displacement of oxygen by Zn^{2+}, that occurs mostly in the carboxyl deprotonated groups and hydroxyl groups [67], but also at the bridge sites between two carbons and onto the center of the hexagonal ring which includes the epoxy functional groups of GO [68, 69], which agree with the observed distribution of ZnO nanoparticles in the TEM micrographs; and (ii) an oxidation of the seeds at high temperature. Additional nucleation and growth shall occur upon excess of Zn in the solution, which explains the observed crystal agglomerations in the SEM micrographs.

The detailed mechanisms are as follows: first, Zn-rGO seeds form onto the negatively charged functional groups of GO, C–OH and COOH. As mentioned above, the reported reduction potential of the hydroxyl groups attached to GO is from $E^0 = -0.4$ to $E^0 = -0.8$ V. The reduction potential of hydroxyl groups of GO is so nearby to that of Zn^0/Zn^{2+}, that a galvanic displacement of the oxygen groups occurs and the Zn^{2+} displaces the oxygen groups and attach to graphene sheet, then seeds start the nucleation by the oxidation at high temperature and then the nuclei grow by the arrival of more Zn^{2+} [70–72]. The observed morphology of the decorated sheet is in agreement with this mechanism. A second mechanism includes the displacement of epoxy groups by Zn^{2+} ions and then the nucleation of $Zn(OH)_2$ and the reduction to ZnO by action of the temperature and then the growth of crystals [73–76], this spontaneous reactions leads the fast nucleation and growth of ZnO crystals. The

overall mechanism is illustrated in the figure 10. Additionally, some ZnO crystals formed in the solution, could precipitate onto the ZnO–rGO compound or may nucleate onto the already formed crystals, as observed by SEM. Future work is intended to study the Zn concentration effect from limiting conditions to determine the nucleation rates and to obtain materials with different ZnO coverage to assess the effect on the electrochemical properties.

4. Conclusions

In this work ZnO–rGO powders were produced by a novel, single-pot procedure involving mild heating and argon flowing in a GO suspension with galvanized iron steel scrap. Graphene oxide is largely reduced. The produced ZnO–rGO has an excellent ZnO crystallinity in wurtzite phase. A stable capacitive behavior was observed by cyclic voltammetry with a specific capacitances of 4.7 to 0.8 F g^{-1}; by EIS measurements a low series resistance, a pseudocapacitive performance, good electron transfer charge, ion diffusion and relaxation time (4.95 ms) of the material was observed. The proposed mechanism included the galvanic displacement of the oxygen groups in the GO sheet, Zn nucleation and ZnO growth.

Acknowledgments

Financed thru the SIP-IPN 20211513 and CONACYT 40798 projects. R. V. Tolentino-Hernandez was financed by CONACYT Master and by BEIFI-IPN grants. Authors thank L. B. Orozco-Solorio for FTIR measurements; to S. A. Pacheco-Buendia for technical support in XRD acquisition; to Dr. R Rangel-Mendez at IPICYT for the access to LINAN facilities for SEM acquisition; to Dr Ma Lourdes Palma Tirado at Unidad de Microscopía, Instituto de Neurobiología UNAM Juriquilla, for TEM acquisition. Authors acknowledge Dr M. Pacio Castillo (CIDS–BUAP) for the facilities provided for diffuse reflectance measurements and Raman acquisition.

Data availability statement

The data that support the findings of this study are available upon reasonable request from the authors.

Conflicts of interest

None.

Author contributions

R V T H prepared the materials, processed, and analyzed the data and wrote the draft; C G A provided access to the Raman characterization facilities and processed the UV–vis data; E J M discussed the results and revised the English language and the final manuscript; F J E F performed the electrochemical characterization. F C B conceived the experiments, co-wrote the draft and revised the final version.

ORCID iDs

R V Tolentino-Hernandez https://orcid.org/0000-0002-9725-8037
F J Espinosa-Faller https://orcid.org/0000-0003-2324-6014
F Caballero-Briones https://orcid.org/0000-0003-4340-1050

References

[1] Hong W, Xu Y, Lu G, Li C and Shi G 2008 Transparent graphene/PEDOT–PSS composite films as counter electrodes of dye-sensitized solar cells *Electrochem. Commun.* **10** 1555–8
[2] Zhao L, Zhao L, Xu Y, Qiu T, Zhi L and Shi G 2009 Polyaniline electrochromic devices with transparent graphene electrodes *Electrochim. Acta* **55** 491–7
[3] Qurashi A, Subrahmanyam K S and Kumar P 2015 Nanofiller graphene–ZnO hybrid nanoarchitecture: optical, electrical and optoelectronic investigation *J. Mater. Chem.* C **3** 11959–64
[4] Fowler J D, Allen M J, Tung V C, Yang Y, Kaner R B and Weiller B H 2009 Practical chemical sensors from chemically derived graphene *ACS Nano* **3** 301–6
[5] Mohamed M M, Ghanem M A, Reda S M, Khairy M, Naguib E M and Alotaibi N H 2019 Photovoltaic and capacitance performance of low-resistance ZnO nanorods incorporated into carbon nanotube-graphene oxide nanocomposites *Electrochim. Acta* **307** 430–41

[6] Ke Q and Wang J 2016 Graphene-based materials for supercapacitor electrodes—a review *J. Mater.* **2** 37–54
[7] Dikin D A, Stankovich S, Zimney E J, Piner R D, Dommett G H B, Evmenenko G, Nguyen S T and Ruoff R S 2007 Preparation and characterization of graphene oxide paper *Nature* **448** 457–60
[8] Yazyev O V and Katsnelson M I 2008 Magnetic correlations at graphene edges: basis for novel spintronics devices *Phys. Rev. Lett.* **100** 47209
[9] Luo D, Zhang G, Liu J and Sun X 2011 Evaluation criteria for reduced graphene oxide *J. Phys.Chem. C* **115** 11327–35
[10] Iwan A, Caballero-Briones F, Bogdanowicz K A, Barceinas-Sánchez J D O, Przybyl W, Januszko A, Baron-Miranda J A, Espinosa-Ramirez A P and Guerrero-Contreras J 2018 Optical and electrical properties of graphene oxide and reduced graphene oxide films deposited onto glass and Ecoflex® substrates towards organic solar cells *Adv. Mater. Lett.* **9** 58–65
[11] De Silva K K H, Huang H-H, Joshi R K and Yoshimura M 2017 Chemical reduction of graphene oxide using green reductants *Carbon* **119** 190–9
[12] Mei X and Ouyang J 2011 Ultrasonication-assisted ultrafast reduction of graphene oxide by zinc powder at room temperature *Carbon* **49** 5389–97
[13] Liu P, Huang Y and Wang L 2013 A facile synthesis of reduced graphene oxide with Zn powder under acidic condition *Mater. Lett.* **91** 125–8
[14] Sarkar S and Basak D 2013 The reduction of graphene oxide by zinc powder to produce a zinc oxide-reduced graphene oxide hybrid and its superior photocatalytic activity *Chemical Physics Letters 561–* **562** 125–30
[15] Guerrero-Contreras J and Caballero-Briones F 2015 Graphene oxide powders with different oxidation degree, prepared by synthesis variations of the Hummers method *Mater. Chem. Phys.* **153** 209–20
[16] Feng Y, Feng N, Weia Y and Zhanga G 2014 An *in situ* gelatin-assisted hydrothermal synthesis of ZnO–reduced graphene oxide composites with enhanced photocatalytic performance under ultraviolet and visible light *RSC Adv.* **4** 7933–43
[17] Liu S, Sun H, Suvorova A and Wang S 2013 One-pot hydrothermal synthesis of ZnO-reduced graphene oxide composites using Zn powders for enhanced photocatalysis *Chem. Eng. J.* **229** 533–9
[18] Ghotbi M Y 2010 Synthesis and characterization of nano-sized ε-$Zn(OH)_2$ and its decomposed product, nano-zinc oxide *J. Alloys Compd.* **491** 420–2
[19] Yan-Li C, Zhong-Ai H, Yan-Qin C, Huan-Wen W, Zi-Yu Z, Yu-Ying Y and Hong-Ying W 2011 Zinc oxide/reduced graphene oxide composites and electrochemical capacitance enhanced by homogeneous incorporation of reduced graphene oxide sheets in zinc oxide matrix *The Journal of Physical Chemistry* C **115** 2563–71
[20] Wei D, Liu Y, Zhang H, Huang L, Wu B, Chen J and Yu G 2009 Scalable synthesis of few-layer graphene ribbons with controlled morphologies by a template method and their applications in nanoelectromechanical switches *J. Am. Chem. Soc.* **131** 11147–54
[21] Yang D *et al* Chemical analysis of graphene oxide films after heat and chemical treatments by X-ray photoelectron and Micro-Raman spectroscopy *Carbon* **47** 2009 145–52
[22] Zhang L, Shi Z, Wang Y, Yang R, Shi D and Zhang G 2011 Catalyst-free growth of nanographene films on various substrates. *Nano Res.* **4** 315–21
[23] Ni Z H, Wang H M, Kasim J, Fan H M, Yu T, Wu Y H, Feng Y P and Shen Z X 2007 Graphene thickness determination using reflection and contrast spectroscopy *Nano Lett.* **7** 2758–63
[24] Pal S, Gogurla N, Das A, Singha S S, Kumar P, Kanjilal D, Singha A, Chattopadhyay S, Jana D and Sarkar A 2018 Clustered vacancies in ZnO: chemical aspects and consequences on physical properties *J. Phys. D* **51** 105107
[25] Cusco R, Alarcon-Llado E, Ibanez J, Artus L, Jimenez J, Wang B and Callahan M J 2007 Temperature dependence of Raman scattering in ZnO *Phys. Rev.* B **75** 165202
[26] Tuinstra F and Koenig J L 1970 Raman spectrum of graphite *J. Chem. Phys.* **53** 1126
[27] Zhang Q, Tian C, Wu A, Tan T, Sun L, Wang L and Fu H 2012 A facile one-pot route for the controllable growth of small sized and well-dispersed ZnO particles on GO-derived graphene *J. Mater. Chem.* **22** 11778–84
[28] Moussa H, Girot E, Mozet K, Alem H, Medjahdi G and Schneider R 2016 ZnO rods/reduced graphene oxide composites prepared via a solvothermal reaction for efficient sunlight-driven photocatalysis *Appl. Catalysis B* **185** 11–21
[29] Jilani A, Abdel-Wahab M S, Zahran H Y, Yahia I S and Al-Ghamdi A A 2016 Linear and nonlinear optical investigations of nano-scale Si-doped ZnO thin films: spectroscopic approach *Appl. Phys.* A **122** 862
[30] Brandstetter S, Derlet P M, Van Petegem S and Swygenhoven H V 2008 Williamson–Hall anisotropy in nanocrystalline metals: x-ray diffraction experiments and atomistic simulations *Acta Mater.* **56** 165–76
[31] Zak A K, Majid W A, Abrishami M E and Yousefi R 2011 X-ray analysis of ZnO nanoparticles by Williamson-Hall and size-strain plot methods *Solid State Sci.* **13** 251–6
[32] Londhe P U and Chaure N B 2017 Effect of pH on the properties of electrochemically prepared ZnO thin films *Mater. Sci. Semicond. Process.* **60** 5–15
[33] Papadimitriou D N 2016 Structural, optical, electrical properties, and strain/stress of electrochemically deposited highly doped ZnO layers and nanostructured ZnO antireflective coatings for cost-effective photovoltaic device technology *Thin Solid Films* **605** 215–31
[34] Sharma P, Kumar N, Chauhan R, Singh V, Srivastava V C and Bhatnagar R 2020 Growth of hierarchical ZnO nano flower on large functionalized rGO sheet for superior photocatalytic mineralization of antibiotic *Chem. Eng. J.* **392** 123746
[35] Obeid M M, Jappor H R, Al-Marzoki K, Al-Hydary I A, Edrees S J and Shukur M M 2019 Unraveling the effect of Gd doping on the structural, optical, and magnetic properties of ZnO based diluted magnetic semiconductor nanorods *RSC Adv.* **9** 33207–21
[36] Caballero-Briones F, Barón-Miranda J A, Guarneros-Aguilar C, Calzadilla O and Sanz F 2019 Influence of pulse frequency on the morphology, structure and optical properties of ZnO films prepared by pulsed electrodeposition *Mater. Res. Express* **6** 086464
[37] Barón-Miranda J A, Calzadilla O, San-Juan-Hernández S, Diez-Pérez I, Díaz J, Sanz F, Chále-Lara F F, Espinosa-Faller F J and Caballero-Briones F 2018 Influence of texture on the electrical properties of Al-doped ZnO films prepared by ultrasonic spray pyrolysis *J. Mater. Sci.: Mater. Electron.* **29** 2016–25
[38] Kumar M, Kumar A and Abhyankar A C 2015 Influence of texture coefficient on surface morphology and sensing properties of W-Doped Nanocrystalline tin oxide thin films *ACS Appl. Mater. Interfaces* **7** 3571–80
[39] Kumar S, Asokan K, Singh R K, Chatterjee S, Kanjilalb D and Ghosh A K 2014 Investigations on structural and optical properties of ZnO and ZnO:Co nanoparticles under dense electronic excitations *RSC Adv.* **4** 62123–31
[40] Mandal S K *et al* Engineering of ZnO/rGO nanocomposite photocatalyst towards rapid degradation of toxic dyes *Mater. Chem. Phys.* **223** 2019 456–65
[41] Zhan Z, Zheng L, Pan Y, Suna G and Li L 2012 Self-powered, visible-light photodetector based on thermally reduced graphene oxide–ZnO (rGO–ZnO) hybrid nanostructure *J. Mater. Chem.* **22** 2589–95

[42] Fan W, Lai Q, Zhang Q and Wang Y 2011 Nanocomposites of TiO_2 and reduced graphene oxide as efficient photocatalysts for hydrogen evolution *J. Phys. Chem.* C **115** 10694–701
[43] Caballero-Briones F, Palacios-Padros A, Calzadilla O, de I, Moreira P R and Sanz F 2012 Disruption of the Chemical environment and electronic structure in p-Type Cu_2O Films by alkaline doping *J. Phys. Chem.* C **116** 13524–35
[44] Jilani A, Othman M H D, Ansari M O, Kumar R, Alshahrie A, Ismail A, Khan I U, Sajit V and Barakat M A 2017 Facile spectroscopic approach to obtain the optoelectronic properties of few-layered graphene oxide thin films and their role in photocatalysis *New J. Chem.* **41** 14217–27
[45] Kashinath L, Namratha K, Srikantaswamy S, Vinub A and Byrappa K 2017 Microwave treated sol–gel synthesis and characterization of hybrid ZnS–RGO composites for efficient photodegradation of dyes *New J. Chem.* **41** 1723–35
[46] Bramhaiah K, Singh V N and John N S 2016 Hybrid materials of ZnO nanostructures with reduced graphene oxide and gold nanoparticles: enhanced photodegradation rates in relation to their composition and morphology *Phys. Chem. Chem. Phys.* **18** 1478–86
[47] Luo Z, Lu Y, Somers L A and Johnson A T C 2009 High yield preparation of macroscopic graphene oxide membranes *J. Am. Chem. Soc.* **131** 898–9
[48] Dave K and Dhayal M 2017 Fluorometric estimation of amino acids interaction with colloidal suspension of FITC functionalized graphene oxide nanoparticles *Appl. Surf. Sci.* **396** 978–85
[49] Selvakumar M and Bhat D K 2012 Microwave synthesized nanostructured TiO_2-activated carbon composite electrodes for supercapacitor *Appl. Surf. Sci.* **263** 236–41
[50] Rajagopal R and Kwang-Sun R 2018 Synthesis of rGO-doped Nb_4O_5–TiO_2 nanorods for photocatalytic and electrochemical energy storage applications *Appl. Catalysis* B **236** 125–39
[51] Rajagopal R, Kamaludeen B A and Krishnan R 2015 Synthesis and exploration of graphene bubbles for supercapacitor electrodes *Electrochim. Acta* **180** 53–63
[52] Chen W, Zhang H, Huang Y and Wang W 2010 A fish scale based hierarchical lamellar porous carbon material obtained using a natural template for high performance electrochemical capacitors *J. Mater. Chem.* **20** 4773–5
[53] Ji-Young K, Kwang-Heon K, Seung-Beom Y, Hyun-Kyung K, Sang-Hoon P and Kwang-Bum K 2013 *In situ* chemical synthesis of ruthenium oxide/reduced graphene oxide nanocomposites for electrochemical capacitor applications *Nanoscale* **5** 6804–11
[54] Shao Y, Wang J, Engelhard M, Wanga C and Lin Y 2010 Facile and controllable electrochemical reduction of graphene oxide and its applications *J. Mater. Chem.* **20** 743–8
[55] Mishra N, Shinde S, Vishwakarma R, Kadam S, Sharon M and Sharon M 2013 MWCNTs synthesized from waste polypropylene plastics and its application in super-capacitors *AIP Conf. Proc.* **1538** 228
[56] Sahu V, Goel S, Sharma R K and Singh G 2015 Zinc oxide nanoring embedded lacey graphene nanoribbons in symmetric/asymmetric electrochemical capacitive energy storage *Nanoscale* **7** 20642–51
[57] Murali A, Sarswat P K and Free M L 2020 Minimizing electron-hole pair recombination through band-gap engineering in novel ZnO-CeO_2-rGO ternary nanocomposite for photoelectrochemical and photocatalytic applications *Environ Sci Pollut Res* **27** 25042–56
[58] Xie X, Yang Z, Feng Z, Zhang Z and Huang J 2015 Electrochemical properties of ZnO added with Zn-Al-hydrotalcites as anode materials for Zinc/Nickel alkaline secondary batteries *Electrochim. Acta* **154** 308–14
[59] Ghorbani M, Golobostanfard M R and Abdizadeh H 2017 Flexible freestanding sandwich type ZnO/rGO/ZnO electrode for wearable supercapacitor *Appl. Surf. Sci.* **419** 277–85
[60] Lopes T, Andrade L, Ribeiro H A and Mendes A 2010 Characterization of photoelectrochemical cells for water splitting by electrochemical impedance spectroscopy *Int. J. Hydrogen Energy* **35** 11601–8
[61] Liu W W, Feng Y Q, Yan X B, Chen J T and Xue Q J 2013 Superior micro-supercapacitors based on graphene quantum dots *Adv. Funct. Mater.* **23** 4111–22
[62] Gul H, Shah A U H A, Krewer U and Bilal S 2020 Study on direct synthesis of energy efficient multifunctional polyaniline–graphene oxide Nanocomposite and its application in aqueous symmetric supercapacitor devices *Nanomaterials* **10** 118
[63] Vu T N, Volovitch P and Ogle K 2013 The effect of pH on the selective dissolution of Zn and Al from Zn–Al coatings on steel *Corros. Sci.* **67** 42–9
[64] Yoshida T, Komatsu D, Shimokawa N and Minoura H 2004 Mechanism of cathodic electrodeposition of zinc oxide thin films from aqueous zinc nitrate baths *Thin Solid Films* **451–452** 166–9
[65] Lincot D 2005 Electrodeposition of semiconductors *Thin Solid Films* **487** 40–8
[66] Riedel W, Tang Y, Ohm W, Chen J, Lux-Steiner M C and Gledhill S 2015 Effect of initial galvanic nucleation on morphological and optical properties of ZnO nanorod arrays *Thin Solid Films* **574** 177–83
[67] Chen D, Zhao Y, Chen Y, Wang B, Chen H, Zhou J and Liang Z 2015 One-Step chemical synthesis of ZnO/Graphene oxide molecular hybrids for high-temperature thermoelectric applications *ACS Appl. Mater. Interfaces* **7** 3224–30
[68] Chandrasekaran S, Chung J S, Kim E J and Hur S H 2016 Exploring complex structural evolution of graphene oxide/ZnO triangles and its impact on photoelectrochemical water splitting. *Chem. Eng. J.* **290** 465–76
[69] Han P, Wang H, Liu Z, Chen X, Ma W, Yao J, Zhu Y and Cui G 2011 Graphene oxide nanoplatelets as excellent electrochemical active materials for VO^{2+}/VO^{2+} and V^{2+}/V^{3+} redox couples for a vanadium redox flow battery *Carbon* **49** 693–700
[70] Toh S Y, Loh K S, Kamarudin S K and Wan Daud W R 2014 Graphene production via electrochemical reduction of graphene oxide: synthesis and characterisation *Chem. Eng. J.* **251** 422–34
[71] Bora C and Dolui S K 2012 Fabrication of polypyrrole/graphene oxide nanocomposites by liquid/liquid interfacial polymerization and evaluation of their optical, electrical and electrochemical properties *Polymer* **53** 923–32
[72] Xiong H and Jin B 2011 The electrochemical behavior of AA and DA on graphene oxide modified electrodes containing various content of oxygen functional groups *J. Electroanal. Chem.* **661** 77–83
[73] Viinikanoja A, Wang Z, Kauppilaac J and Kvarnström C 2012 Electrochemical reduction of graphene oxide and its *in situ* spectroelectrochemical characterization *Phys. Chem. Chem. Phys.* **14** 14003–9
[74] Song W, Han X, Chen L, Yang Y, Tang B, Ji W, Ruan W, Xu W, Zhao B and Ozaki Y 2010 Site-specific deposition of Ag nanoparticles on ZnO nanorod arrays via galvanic reduction and their SERS applications *J. Raman Spectrosc.* **41** 907–13
[75] Mondal A, Mukherjee N and Bhar S K 2006 Galvanic deposition of hexagonal ZnO thin films on TCO glass substrate *Mater. Lett.* **60** 1748–52
[76] Chen Y L, Hu Z A, Chang Y Q, Wang H W, Zhang Z Y, Yang Y Y and Wu H Y 2011 Zinc Oxide/Reduced graphene oxide composites and electrochemical capacitance enhanced by homogeneous incorporation of reduced graphene oxide sheets in Zinc Oxide matrix *The Journal of Physical Chemistry* C **115** 2563–71